Energy &
Environmental
Science

**ROYAL SOCIETY
OF CHEMISTRY**

PAPER
Guanjie He *et al.*
Identification and manipulation of dynamic active site
deficiency-induced competing reactions in electrocatalytic
oxidation processes

PAPER

Check for updates

Identification and manipulation of dynamic active site deficiency-induced competing reactions in electrocatalytic oxidation processes†

Runjia Lin, [ID] [a] Liqun Kang, [ID] [b] Tianqi Zhao, [ID] [a] Jianrui Feng, [c] Veronica Celorrio, [ID] [d] Guohui Zhang, [e] Giannantonio Cibin, [d] Anthony Kucernak, [ID] [e] Dan J. L. Brett, [ID] [b] Furio Corà, [ID] [a] Ivan P. Parkin [ID] [a] and Guanjie He [ID] *[abf]

Electrocatalytic organic compound oxidation reactions (OCORs) have been intensively studied for energy and environmentally benign applications. However, relatively little effort has been devoted to developing a fundamental understanding of OCORs, including the detailed competition with side reactions and activity limitations, thus inhibiting the rational design of high-performance electrocatalysts. Herein, by taking the $NiWO_4$-catalysed urea oxidation reaction (UOR) in aqueous media as an example, the competition between the OCOR and the oxygen evolution reaction (OER) within a wide potential range is examined. It is shown that the root of the competition can be ascribed to insufficient surface concentration of dynamic Ni^{3+}, an active site shared by both the UOR and OER. A similar phenomenon is observed in other OCOR electrocatalysts and systems. To address the issue, a "controllable reconstruction of pseudo-crystalline bimetal oxides" design strategy is proposed to maximise the dynamic Ni^{3+} population and manipulate the competition between the UOR and the OER. The optimised electrocatalyst delivers best-in-class performance and an ~10-fold increase in current density at 1.6 V *versus* the reversible hydrogen electrode for alkaline urea electrolysis compared to those of the pristine materials.

Broader context

Electrocatalytic oxidation processes such as the oxygen evolution reaction (OER) are particularly critical for harvesting and utilising renewable energy. Despite enormous efforts, the inherently sluggish OER raises concerns towards the industrialization of electrochemical-based technologies. Electrocatalytic organic compound oxidation reactions (OCORs) have been intensively studied due to their lower overpotentials and capability to decompose organic pollutants. Though significant efforts have been made for advancing the performance (onset potential and oxidation current) of OCORs, understanding of their mechanism is still limited. Importantly, a majority of OCORs share the potential window and/or catalyst design principles with the OER, which will result in a detrimental competition. Here, we discover the existence of a competition between the urea oxidation reaction (UOR) and the OER which gives rise to a current cut-off during electrocatalytic process governed by $NiWO_4$-based catalysts. Through experiments, computational calculations and *operando* observations, the low concentration of dynamic Ni^{3+} is identified as the root cause. A controllable pre-activation approach is proposed to create abundant, recyclable and dynamic active sites, and dislocate the potential window of the UOR/OER by modifying the binding strengths of the reaction intermediates. Consequently, the UOR/OER performance saturation can be avoided, leading to an increased UOR performance. Furthermore, similar phenomena were observed in methanol and ethanol oxidation reactions.

[a] *Christopher Ingold Laboratory, Department of Chemistry, University College London, 20 Gordon Street, London WC1H 0AJ, UK. E-mail: g.he@ucl.ac.uk*

[b] *Department of Chemical Engineering, University College London (UCL), London, WC1E 7JE, UK*

[c] *Key Laboratory of Advanced Energy Materials Chemistry (Ministry of Education) and the Tianjin Key Lab and Molecule-based Material Chemistry, College of Chemistry, Nankai University, Tianjin 300071, China*

[d] *Diamond Light Source Ltd, Diamond House, Harwell Campus, Didcot, OX11 0DE, UK*

[e] *Department of Chemistry, Imperial College London, South Kensington Campus, London SW7 2AZ, UK*

[f] *School of Chemistry, University of Lincoln, Brayford Pool, Lincoln, LN6 7TS, UK*

† Electronic supplementary information (ESI) available. See DOI: 10.1039/d1ee03522c

2386 | *Energy Environ. Sci.,* 2022, **15**, 2386–2396

This journal is © The Royal Society of Chemistry 2022

Introduction

Promoting the transition of global energy consumption from fossil fuels to a renewable energy-dominated pattern requires replacing traditional fuel utilisation devices with novel energy storage and conversion technologies.[1–3] The development of advanced electrocatalytic oxidation processes is particularly critical for improving the utilization of renewable energy.[4,5] The most widely investigated anodic reaction is the oxygen evolution reaction (OER). Despite enormous efforts, the inherently sluggish OER kinetics requires excessive overpotentials to drive water electrolysers for hydrogen production.[6] In addition, the low economic value of O_2 compared to that of H_2 limits the overall benefit of the water splitting process. To address these issues, organic compound oxidation reactions (OCORs), such as urea, methanol and ethanol oxidation reactions (UOR, MOR, and EOR), that require lower overpotentials and are competent to break down organic pollutants from agricultural/industrial/domestic/aerospace wastes, have been proposed and have achieved considerable progress in terms of electrocatalyst design.[7,8] Though several thought-provoking studies have expanded the discussion of OCORs beyond the comparison of current densities and onset potentials to mechanistic studies (*i.e.* reaction products and rate-limiting step),[9–12] the understanding of reaction selectivity, dynamic active sites/catalyst interfaces and activity limitations is still unclear and requires further comprehensive exploration. Importantly, a majority of OCORs share the potential window and/or catalyst design principles with the OER, which may result in a detrimental competition. Exploring detailed catalytic mechanisms of OCORs, especially when the applied potential is in the conventional OER zone, can open the possibility of rational and efficient design of new anodic reaction electrocatalysts.

The conventional electrocatalyst design strategy established on the assumption of a static electrolyte/electrode interface has recently been challenged by the discovery of materials reconstruction phenomena under operating conditions.[13–15] In particular, it has been found that many metal oxide/perovskite electrocatalysts undergo a surface self-reconstruction from oxides to (oxy)hydroxides after an electrochemical treatment, wherein their catalytical activities can be boosted.[16–18] However, considering the irreversibility of the surface oxyhydroxylation process (since the reconstruction can only be induced at particular circumstances, for example, leaching of metals from specific sites of the catalyst lattice structures),[16] the enhanced activity, which is enabled by the oxyhydroxidized surface, is more like "a flash in the pan" when it comes to high-valence active site-consuming electrocatalytic reactions (*i.e.* UOR).[19] Developing "renewable" high-valence species, for instance, dynamic active centres that can be "recycled" *via* redox reactions, is of great importance for advanced electro–oxidation processes.

Here, by correlating the dynamic phenomena between the catalytic activity and real-time product generation rate of alkaline urea electrolysis on well-designed NiWO$_4$-tannic acid (TA) catalysts, we discover the presence of a detrimental competition between the UOR and the OER, which is responsible for a drop in the potential–current relationship within the competition zone. *Operando* X-ray spectroscopic investigations and theoretical simulations identify that low concentration of dynamic Ni^{3+} is the root cause of the detrimental OER/UOR competition. A controllable pre-activation approach is proposed consisting of electrochemical leaching of tungstate species from pseudo-crystalline NiWO$_4$-TA hybrids to enhance (near)surface-exposed Ni active sites with excellent structural and chemical flexibility, eventually promoting the *in situ* formation of abundant active Ni^{3+} surface species. Computational calculations suggest that these dynamic Ni^{3+} centres decrease the UOR onset potential but increase the OER onset potential compared with that of the conventional Ni–oxyhydroxide surface. In the modified electrocatalysts, the UOR is no longer limited by the competitive OER regardless of the applied potential, which leads to a nearly 10-fold performance improvement in current density at 1.6 V *vs.* the reversible hydrogen electrode (RHE) over its pristine counterpart. Further experimental results suggest that the UOR/OER competition and its corresponding solutions apply to the MOR and a broad sphere of other electrocatalytic systems beyond the OCORs.
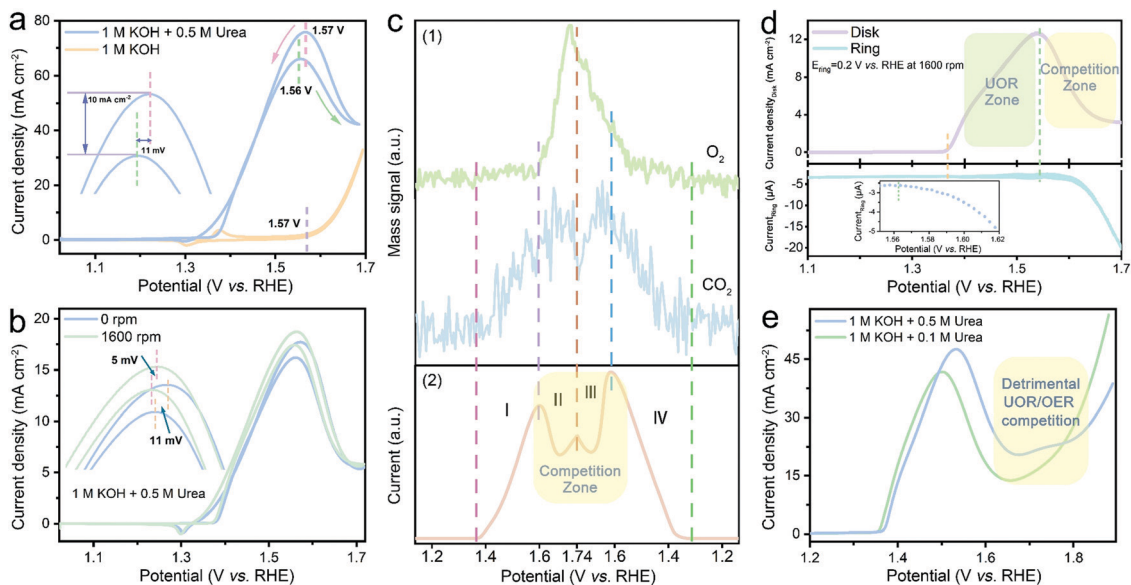
Results

Identification of the UOR/OER competition

A series of NiWO$_4$-based catalysts were prepared; their structural, morphological and chemical information was evaluated by X-ray diffraction (XRD, ESI,† Fig. S1a), transmission electron microscopy (TEM, ESI,† Fig. S1b–i), X-ray photoelectron spectroscopy (XPS, ESI,† Fig. S2) and X-ray absorption fine structure (XAFS) spectroscopy (ESI,† Fig. S3 and S4), respectively. As pseudo-crystalized NiWO$_4$ nanoparticles grown over TA-derived hydrochar frameworks (denoted as NiWO$_4$-TA) showed the best electrochemical response (ESI,† Fig. S5), the dynamic electrocatalytic activity–selectivity trend for alkaline urea electrolysis was first established on this material and the results are summarised in Fig. 1.

Fig. 1a shows the electrocatalytic performance of NiWO$_4$-TA evaluated in 1 M KOH with and without 0.5 M urea. The electro–oxidation of urea begins at ∼1.37 V *vs.* RHE, beyond which the oxidation current increases with the applied voltage (in the low-potential region). Surprisingly, two neighbouring 'anodic peaks', which are centred at ∼1.56 V *vs.* RHE, appear sequentially in the forward and backward scans. Accordingly, the electrolysis does not show a conventional positively-correlated potential–current relationship, thus even exhibiting inferior performance in the high-potential region. The unclear but detrimental 'anodic peaks' were first attributed to the redox chemistry of the catalyst; nevertheless, only a Ni^{2+}/Ni^{3+} redox pair at ∼1.36 V *vs.* RHE can be identified in the cyclic voltammetry (CV) plot obtained in 1 M KOH, which disproves the self-oxidation of the catalysts.

Interestingly, the "anodic peaks" can also be observed when cycling NiWO$_4$-TA in 1 M KOH in the presence of other organic

This journal is © The Royal Society of Chemistry 2022

Energy Environ. Sci., 2022, **15**, 2386–2396 | **2387**

Fig. 1 UOR/OER competition identification based on the electro-oxidation performance of the NiWO4-TA catalyst. (a) CV scan in 1 M KOH aqueous electrolyte with (blue) and without (orange) 0.5 M urea. (b) Comparison of the polarisation curves recorded in 1 M KOH + 0.5 M urea at 0 (blue) and 1600 (green) rpm, respectively. (c) (1) *Operando* monitoring of the representative gaseous products of OER (O_2) and UOR (CO_2) by RTMS and (2) the corresponding electrochemical data acquired in 1 M KOH + 0.5 M urea (scan rate: 10 mV s^{-1}, without *iR* correction). (d) *In situ* evaluation of O_2 production using RRDE, the inset is the enlarged E_{disk}–$I_{current}$ plot near the boundary of UOR and competition zone (disk current was collected by linear sweep voltammetry (LSV) in 1 M KOH + 0.5 M urea electrolyte at 5 mV s^{-1}, further information is available in the ESI,† Fig. S10). (e) LSV curves obtained in 1 M KOH with different concentrations of urea.

compounds, for instance, methanol (ESI,† Fig. S6) and ethanol (ESI,† Fig. S7), revealing that they are most likely the consequence of OCORs. Previous reports suggest that limited mass transfer of chemical species by diffusion to the electrode could cause reactant depletion/product accumulation, thus leading to a current cut-off at a certain voltage (*i.e.* polarisation curves of fuel cell systems).[20,21] To study the effect of mass transfer, the polarisation tests under different rotation rates of 0 and 1600 rpm were performed in 1 M KOH + 0.5 M urea (Fig. 1b and ESI,† Fig. S8); the CVs exhibit no dependence on rotation rates evidencing that the oxidation reaction is not mass transfer limited.

It is noteworthy that the 'anodic peaks', regardless of the test conditions, consistently appear near the onset of the OER (dashed purple lines in Fig. 1a and ESI,† Fig. S6–S8), indicating the possible existence of a competition between OCORs and OER which may trigger the undesired overall activity decay in the OER zone. Real-time mass spectrometry (RTMS) was employed to uncover the dynamic relationship of the OER and the UOR as a function of applied potential by monitoring the real-time intensity of their representative gaseous products O_2 and CO_2 (further information on the cell employed is available in the ESI,† Fig. S9).[22] Different regions are identified, labelled as I–IV in Fig. 1c; in the region I up to 1.6 V *vs.* RHE, the CO_2 partial pressure increases with the oxidation current and the applied voltage, while the O_2 signal remains flat, suggesting that the UOR is the dominant reaction in the low-potential region. As the applied potential increases above 1.6 V (region II), an O_2 intensity surge, together with a sudden drop of CO_2

intensity and overall current drop, occurs simultaneously; this provides evidence for the as-proposed OER/UOR competition. The variation of gas composition and oxidation current in the sequential reverse scan (region III and IV) shows a similar pattern to that in the forward scan (region I and II), confirming that the 'anodic peaks' come from the UOR/OER competition. The same conclusion can be reached from the dynamic overall activity (Fig. 1d upper panel) and O_2 generation rate (lower panel) evaluated using the rotation ring-disk electrode (RRDE) system. No O_2 can be detected by the ring electrode prior to the emergence of the 'anodic peak'; the *in situ* collection of disk-generated O_2 by the ring electrode begins at ∼1.56 V *vs.* RHE (the inset in Fig. 1d) where the activity cut-off takes place (∼1.55 V *vs.* RHE), which agrees with the RTMS results.

To manipulate the kinetics of the OER and the UOR and adjust their competing pattern, electrochemical tests were performed in electrolytes containing various concentrations of the reactants (ESI,† Note 1). Fig. S11 and S12 in the ESI† reveal that a higher OH$^-$ concentration leads not only to more vigorous UOR and OER kinetics but also higher UOR/OER competition. Similarly, as demonstrated in Fig. 1e, the increase of urea concentration leads to a more sluggish electrochemical response in the competition zone, suggesting that the mitigation of the UOR/OER competition cannot be accomplished *via* a straightforward reactant concentration manipulation strategy. The results presented above clearly show that the OER is a strong competitor of the UOR under a wide range of conditions. This competition likely leads to a deterioration of performance of the overall catalytic system. Although the impact of the OER

2388 | *Energy Environ. Sci.*, 2022, **15**, 2386–2396

This journal is © The Royal Society of Chemistry 2022

in OCOR electrolysis has been mentioned in previous reports,[23–25] a comprehensive explanation of the origin of the detrimental competition and a feasible resolution are still uncharted which demands further investigation.

Correlating dynamic Ni active sites with UOR/OER competition

The next step attempted to explore and resolve the origin of the UOR/OER competition and advance the catalyst design. As can be inferred from Fig. 2a, the electrochemical behaviour of the $NiWO_4$-TA catalyst, specifically its Ni^{2+}/Ni^{3+} transition peak and OER activity, evolves dramatically after CV cycling in 1 M KOH. The urea electrolysis performance improves in tandem with electrochemical aging, evidenced by the UOR onset shifting to lower potentials and dramatically enhanced oxidation current

densities (Fig. 2b). More interestingly, there is no current collapse noticed in LSVs of the extensively-cycled samples ($NiWO_4$–$TA_{200\ or\ 950}$), highlighting a profoundly transformed OER–UOR interrelationship occurring on the aged electro-catalyst. It is worth mentioning that the urea electrolysis activity of $NiWO_4$-TA_x stabilises as the number of CV cycles (x) exceeds 950 (ESI,† Fig. S13). A similar trend can also be observed for other as-synthesised $NiWO_4$-based catalysts but with different evolution momentum due to the variation in crystallinity which will be discussed in detail later (ESI,† Fig. S46–S54).

According to previous literature trace amount of Fe ions in the electrolyte could participate in the surface reconstruction of (oxy)hydroxide materials, which consequently influenced the catalytic behaviour.[26,27] To explore this possibility, a control
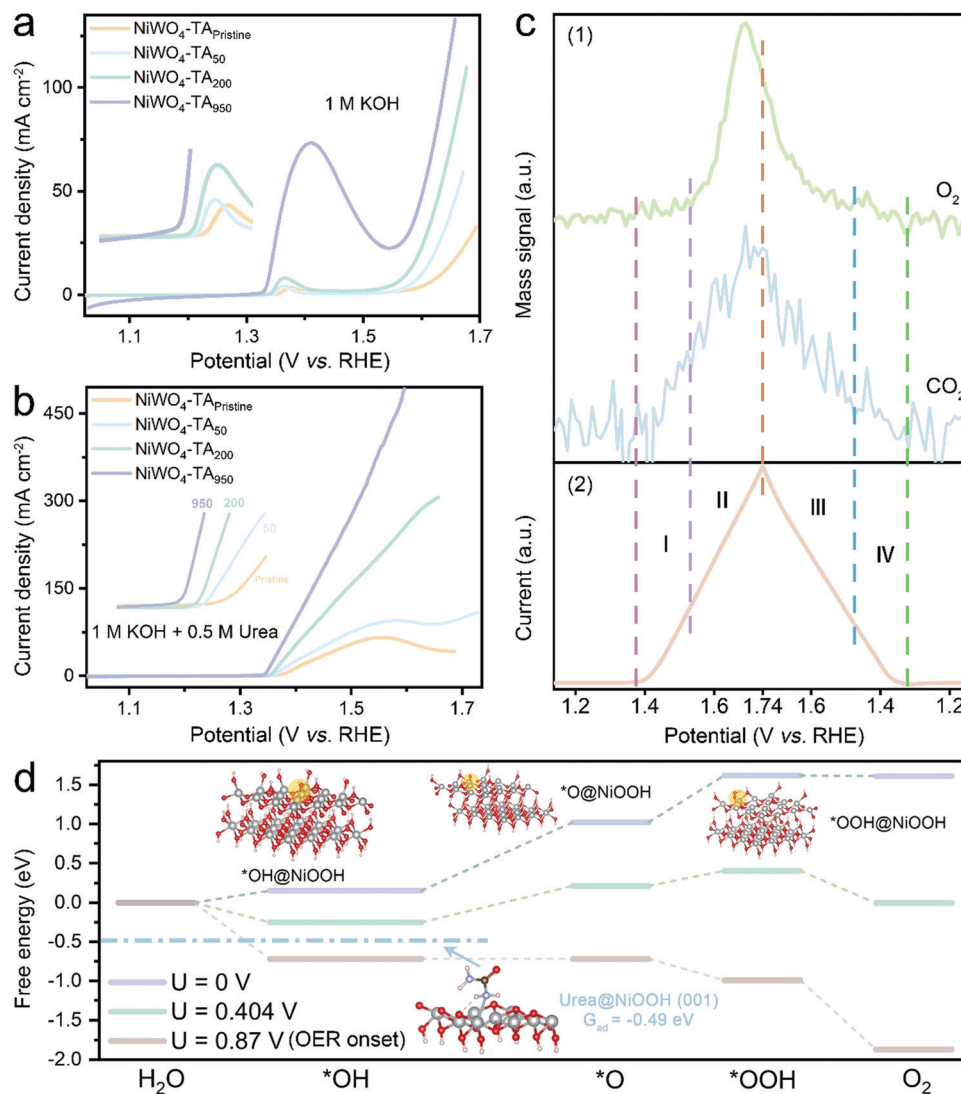
Fig. 2 Root cause identification and resolution exploration for UOR/OER competition. (a and b) LSVs of $NiWO_4$–TA_x (x represents the number of CV cycle treatment conducted in 1 M KOH before the water or urea electrolysis test) evaluated in (a) 1 M KOH and (b) 1 M KOH + 0.5 M urea. (c) (1) *Operando* monitoring of the representative gaseous products of the $NiWO_4$–TA_{950}-catalysed OER (O_2) and UOR (CO_2) by RTMS and (2) the corresponding electrochemical data acquired in 1 M KOH + 0.5 M urea (scan rate: 10 mV s^{-1}, without *iR* correction). (d) Comparison of the adsorption chemistry of urea and *OH over the NiOOH (001) surface at different applied potentials and free energy diagram of the OER over the NiOOH (001) surface at potentials of 0 (purple), 0.404 V (green) and 0.87 V (pink) *vs.* normal hydrogen electrode (NHE).

experiment was conducted and the results shown in Fig. S14, ESI† suggest that the influence from trace Fe ions (in the electrolyte) can be ignored in this work. The disappearance of the current collapse phenomenon was then assigned to the ever-increasing OER activity that is eventually capable of compensating the UOR current cut-off. However, as shown in Fig. S15 ESI,† the current density difference between the urea and water electrolysis systems widens with the pre-activation degree of the catalysts, which rules out the role of OER activity increase as a cause for the disappearance of the current cut-off. Considering the pronounced electrochemical behaviour transformation of $NiWO_4$–TA_{950} compared to that of $NiWO_4$–$TA_{Pristine}$, it is important to unravel an updated UOR–OER relationship to explain the quasi-exponential LSV curve of urea electrolysis (Fig. 2b). RTMS was performed, and the outcome is displayed in Fig. 2c. Surprisingly, the partial pressure of CO_2 shows a direct correlation with the applied potential throughout the scan, which differs greatly from the results shown in Fig. 1c for the pristine catalyst. In addition, the detection of O_2 at high potential confirms the contribution of the OER to the overall oxidation current. The CO_2/O_2 intensity variation observed for $NiWO_4$–TA_{950} allows us to emphasize two important features of the activated catalyst: first, the UOR escapes the influence of the OER, thus avoiding the current collapse; second, the UOR and OER coexist rather than being mutually exclusive.

To explain the evolved UOR/OER relationship, attention was then directed to the *in situ* Ni chemistry of $NiWO_4$–TA_x. As presented in Fig. S16, ESI,† a clear enhancement of the redox peak at ~1.34 V *vs.* RHE assigned to $Ni^{2+/3+}$ oxidation upon cycling can be witnessed. This indicates an increased concentration of redox-active Ni (that is referred to as dynamic Ni^{3+}), which is a cause for the enhanced activity. In other words, the root of the UOR/OER saturation can be attributed to the insufficient concentration of dynamic Ni^{3+} active sites. To establish a comprehensive understanding of the relationship between Ni^{3+}, UOR and OER, density functional theory (DFT) calculations were carried out to determine the adsorption energy of several key UOR/OER intermediates on NiOOH whose (001) plane is regarded as a representative Ni^{3+}-rich model for catalytic studies (even though calculations on $NiWO_4$ performed here indicated that the actual dynamic Ni coordination in our pristine/aged catalysts may be more complex).[28,29] As illustrated in Fig. 2d and in the ESI,† Note S2, Fig. S17, the adsorption energy of urea on NiOOH is calculated to be −0.49 eV which is much lower than that of *OH under moderate bias. Accordingly, the influence of the OER on the oxidation of urea by Ni^{3+} is negligible. However, as the applied potential further increases, *OH gradually takes a more favourable position over urea in terms of occupying Ni^{3+} sites, resulting in a Ni^{3+} 'crisis' for UOR. The Ni^{3+} deficiency problem is further exacerbated by the sluggish OER kinetics, especially the elementary step (*OH → *O). In other words, *OH effectively 'poisons' the Ni^{3+} active sites by preferentially absorbing but slowly reacting with them. Subsequently, a UOR current cut-off occurs due to the limited number of Ni^{3+} sites left available for urea molecules. On the other hand, the saturation

of redox-active Ni at the basis of the UOR/OER competition can be avoided, should the concentration of dynamic Ni^{3+} be increased.

Operando measurement of the Ni oxidation state

To verify the role of Ni^{3+} in the OER and the UOR, *operando* X-ray absorption near edge structure (XANES) measurements were performed (further information on the experiment setup is available in Fig. S18, ESI†). As presented in Fig. 3a and Fig. S19a, ESI,† during the OER of aged electrodes in KOH, accumulation of Ni^{3+} becomes noticeable from ~1.45 V *vs.* RHE in the anodic scan, and the Ni^{3+} concentration remains high (~20%) at higher applied voltages. The positive Ni^{3+} composition-applied potential relationship suggests the formation rate of high valence Ni is higher than its consumption rate (by the OER). The accumulated Ni^{3+} sites can be classified into two categories: those occupied by OER intermediates, and those that remain unoccupied. In the presence of urea, the latter Ni^{3+} sites are able to catalyse the UOR, thus preventing the current collapse in the OER zone. According to Fig. 3b and Fig. S19b, ESI,† the signal of Ni^{3+} species is nearly negligible throughout the entire urea electrolysis scan, indicating the consumption of the 'free' Ni^{3+} by the UOR. Contrarily, owing to its inactive Ni redox chemistry, only a trace amount of Ni^{3+} can be found during the OER of the pristine catalyst (ESI,† Fig. S20a and S21a). Accordingly, a limited amount of unoccupied Ni^{3+} is available for the UOR, leading to the current collapse (ESI,† Fig. S20b and S21b). The observed *operando* XANES results validate the hypothesis that dynamic Ni^{3+} species are shared active sites for both OER and UOR and their deficiency causes the observed OER/UOR competition. It is noteworthy that no noticeable change can be found in the W L_3-edge XANES spectra for both pristine and aged electrodes during either water or urea oxidation electrolysis (ESI,† Fig. S22 and S23) which suggests that W retains the original W^{6+} in the octahedral WO_6 coordination structure in the bulk structure throughout the electrocatalytic cycle.

Due to flexible Ni chemistry, $NiWO_4$–TA_{950} exhibits an ultra-high urea electrolytic activity (~10 times higher current density compared to commercial RuPt/C at 1.6 V *vs.* RHE), favourable kinetics (a low Tafel slope of 26.4 mV dec^{-1}) and outstanding urea utilization capability (ESI,† Fig. S24 and S25). More importantly, our findings are also applicable to methanol electrolysis and ethanol electrolysis (ESI,† Fig. S26 and S27) and could be extended to improve the activity and selectivity of other heterogeneous catalytic processes.

Identification of morphological and coordination chemistry alteration upon cycling

To support the rational design strategy of new anode catalysts, it is vital to unravel the reasons that lead to the enhanced population of dynamic Ni^{3+} active sites in $NiWO_4$–TA_{950}. Earlier studies suggest that Ni-based (hydro)oxide might undergo an irreversible surface amorphization into Ni^{3+}-rich oxyhydroxides under alkaline conditions, thus exhibiting enhanced activities. To examine changes in the morphology of the aged catalyst,
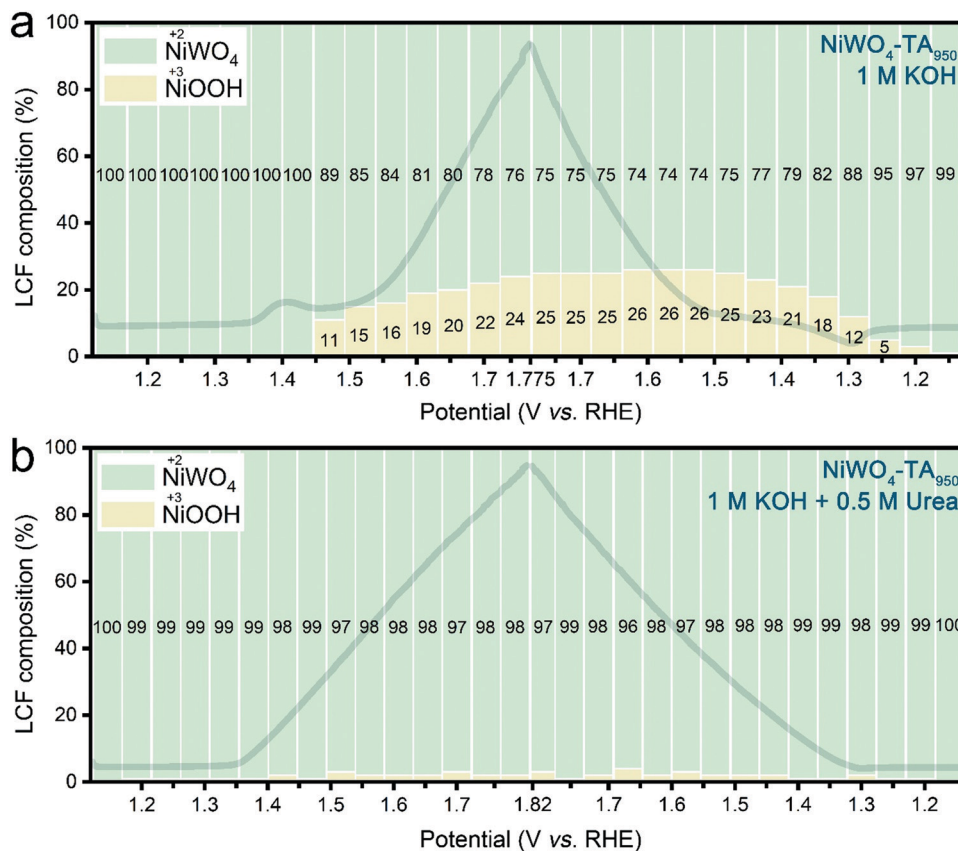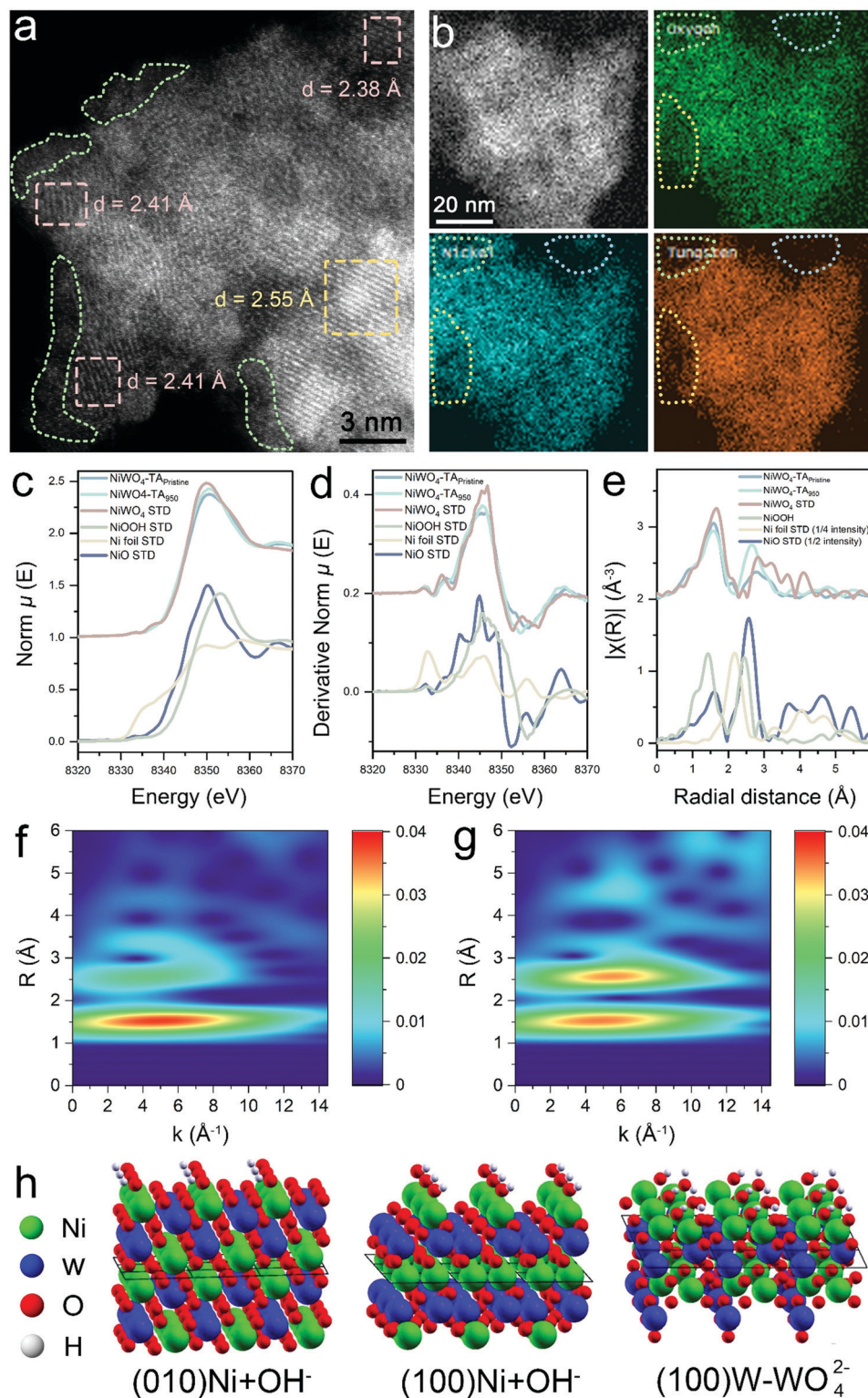
2390 | *Energy Environ. Sci.*, 2022, **15**, 2386–2396

This journal is © The Royal Society of Chemistry 2022

Fig. 3 *Operando* monitoring of the Ni oxidation state of NiWO$_4$–TA$_{950}$ during water and urea electrolysis. Linear combination fitting (LCF) results of Ni K-edge XANES spectra of NiWO$_4$–TA$_{950}$ under *operando* conditions in (a) 1 M KOH and (b) 1 M KOH + 0.5 M urea. The dark lines in the background are the corresponding LSVs without *iR* correction.

high-angle annular dark-field scanning transmission electron microscopy (HAADF-STEM) was performed. As confirmed by the amorphous phase highlighted in the green dot area in Fig. 4a, an oxyhydroxide layer forms after electrochemical treatment,[16,30,31] revealing that NiOOH is likely to be one of the sources of Ni^{3+}. However, electrochemical data displayed in Fig. S28, ESI,† suggests that the contribution of surface oxyhydroxide species to the overall activity of the reconstructed catalyst is almost negligible and non-renewable. It is worth mentioning that surface reconstruction generally takes place only in the first few CV cycles which can be proved by the gradually weakened pseudocapacitive behaviour (ESI,† Fig. S29). However, our observation suggests that no obvious catalytic behaviour alterations of NiWO$_4$–TA can be witnessed until at least dozens or even hundreds of CV cycles have been conducted, indicating the reconstructed NiOOH layer is not a major Ni^{3+} contributor. It has been recently reported that electrochemical leaching of metal species from bulk structures could create pores and boost the electrochemical surface area (ECSA) of the electrode, thus improving the catalytic performance.[32,33] The selective leaching of one element in multicomponent oxides can also alter the surface composition and chemistry. To detect any possible metal leaching, inductively coupled plasma-atomic emission spectroscopy (ICP-AES)

measurements were performed on the electrolyte upon cycling (ESI,† Fig. S30) and demonstrated constant leaching of W cations while the release of Ni cations into solution was negligible. In addition, *ex situ* energy dispersive X-ray spectroscopy (EDS) and XPS results show a reduction in W population in aged samples (Fig. 4b and ESI,† Fig. S31, S32) which agree with the ICP-AES result. The ECSA of the aged catalyst shows a considerable increase (ESI,† Fig. S33 and S34e) which might eventually lead to its more vigorous Ni redox peaks. In other words, the flexible Ni chemistry of the aged samples can be attributed to their enlarged ECSA which accordingly provides more active sites. However, the as-discussed ECSA-enlarging hypothesis is not able to explain the gradually increased dynamic Ni^{3+} formation ability per ECSA (denoted as MPE$_{Ni}$) for NiWO$_4$–TA$_x$ catalysts (ESI,† Fig. S34f) as MPE$_{Ni}$ is mainly governed by the active site type and density on the electrode rather than its ECSA, hence should remain stable. Therefore, the most decisive reason behind the enhanced Ni redox chemistry still remains unclear with no convincing explanation from previous studies.

To evaluate the precise morphological and coordination chemistry changes between the pristine and cycled NiWO$_4$-TA catalyst, *ex situ* EXAFS was performed. As shown in Fig. 4c–g and Fig. S35, ESI,† the coordination environment of Ni has

This journal is © The Royal Society of Chemistry 2022

Energy Environ. Sci., 2022, **15**, 2386–2396 | **2391**

Fig. 4 Clarification of the morphological and coordination chemistry evolution after cycling. (a) HAADF-STEM image and (b) EDS mapping of NiWO$_4$–TA$_{950}$. Ni K-edge (c) XANES, (d) derivative XANES and (e) k^2-weighted R-space EXAFS of NiWO$_4$–TA$_{pristine}$, NiWO$_4$–TA$_{950}$, commercial NiWO$_4$, commercial NiO, commercial NiOOH and commercial Ni foil. (f and g) Ni K-edge k^2-weighted wavelet transform-extended X-ray absorption fine structure spectra of (f) NiWO$_4$–TA$_{Pristine}$ and (g) NiWO$_4$–TA$_{950}$. (h) Optimised Ni-terminated (010) and (100) surfaces with OH$^-$ adsorption, and NiWO-W (100) surface obtained by WO$_4^{2-}$ leaching from the W-terminated (100) surface.

changed significantly after cycling, with nearly the same first shell coordination but a much stronger second shell coordination.

Further fitting results confirmed that Ni maintained its 6-O coordination in the first shell after activation, but the second

2392 | *Energy Environ. Sci.*, 2022, **15**, 2386–2396

This journal is © The Royal Society of Chemistry 2022

shell Ni–W coordination number (C.N.) decreased from 4.0 to 2.7 while the Ni–Ni C.N. increased from 2.0 to 4.9. This is the direct evidence of aggregation of Ni species or formation of a Ni-rich phase. Such a reconstructed phase whose interplane spacing greatly differs from that of the pristine $NiWO_4$ (002) plane, can be identified in the STEM image in Fig. 4a (highlighted as a pink dot area). However, negligible changes can be observed in the W L_3-edge EXAFS spectra of pristine and activated $NiWO_4$, even in the wavelet transform-extended X-ray absorption fine structure (WT-EXAFS) (ESI,† Fig. S36 and S37), indicating that W in the bulk structure of the activated sample retains its original structure as in the pristine sample (highlighted as a yellow dot area in Fig. 4a). Density of states analysis shown in Fig. S38, ESI,† indicates a higher degree of electron delocalisation in the cycled sample. Based on our experimental observations, it is believed that the formed Ni-rich phase outer layer is responsible for the flexible Ni chemistry of $NiWO_4$–TA_{950}. Moreover, the amorphous oxyhydroxide surface layer promotes interphase ion transport (ESI,† Fig. S39), and the enlarged ECSA also contribute to the enhanced catalytic performance of the reconstructed catalyst. Control experiments suggest this unique structure cannot be created without the leaching of W (ESI,† Fig. S40).

To elucidate the W leaching and formation of Ni-rich phases, further DFT calculations were performed on $NiWO_4$ surfaces (ESI,† Note 3). Calculated surface energies indicate that a W rich termination is stable over Ni exposed ones for (100) and (010) surfaces in vacuum, representative of the pristine catalyst (ESI,† Fig. S41). In contact with the highly alkaline 1 M KOH electrolyte, oxidation of the surface Ni^{2+} to Ni^{3+} and concurrent adsorption of one additional hydroxide ion was calculated as exothermic, leading to oxidized $Ni^{3+}(OH)$ surfaces being the stable terminations of the catalyst (Fig. 4h). W leaching as tungstate ions (WO_4^{2-}) from the W-terminated (100) face in an alkaline environment, yielding new $Ni(OH)$ terminations (denoted as the NiWO-W (100) surface, ESI,† Fig. S42), was predicted to be endothermic, but facilitated by the high hydration energy of the doubly negative tungstate ions. Leaching may therefore be expected to occur as a slow, irreversible process. Should all surface Ni be oxidized to the 3+ state and hydroxylated, the surface formation energy for both (010) and (100) surfaces is calculated as negative, suggesting that additional surfaces are generated and the exposed surface area increases upon cycling. Such a process, although energetically feasible is likely to require high activation barriers, hence a large number of CV cycles are needed for it to take place, consistent with the experimental observations. It is worth pointing out that W species, regardless of being leached or preserved, remain at the 6+ oxidation state throughout the cycling process (ESI,† Fig. S43). Assuming the dynamic Ni^{3+} active site in the near-surface region of the activated sample under operation conditions possesses similar coordination to its hydroxidized outer layer structure under static conditions (considering that the adsorption of additional hydroxide ions is the most reasonable explanation for the evolution of the reconstructed near-surface Ni(II)-rich structure to a dynamic Ni(III)-based coordination even though redox chemistry on the near-surface region may be more complex), we then evaluated the adsorption chemistry of the key UOR/OER intermediates on the NiWO-W (100) surface (ESI,† Fig. S44). Similar to the results obtained on the NiOOH (001) surface (Fig. 2d), urea dominates the NiWO-W (100) surface under moderate bias while *OH gradually takes lead in occupying the reconstructed surface with the increase in the applied potential. The UOR process is thermodynamically favourable on both surfaces (ESI,† Fig. S45). It is worth mentioning that the NiWO-W (100) surface exhibits a much lower urea adsorption energy (−1.12 eV) and a higher OER onset (0.991 V *vs.* NHE) compared to those of the NiOOH (001) surface (G_{ad} = −0.49 eV, U_{onset} = 0.87 V *vs.* NHE). In other words, the NiWO-W (100) surface better dislocates the potential window of the UOR and the OER than the NiOOH (001) surface, thus mitigating the possibility of the saturation of redox-active Ni by the OER and the UOR. Though complete suppression of the OER at the high-potential region has still not been accomplished due to the adsorptive nature of OH* (at the high-potential region, as confirmed by the simulation results in this work and previous literature[25]), the postponed OER and advanced UOR on the NiWO-W (100) surface open the possibility of dislocating the UOR/OER by tuning the electronic structures of the catalysts, accordingly modifying the binding strengths of the reaction intermediates.

Control of W leaching kinetics

It is worth mentioning that these series of $NiWO_4$ materials exhibit different W leaching kinetics which can possibly be ascribed to the variation of their crystallinities. As shown in Fig. S46–S51, ESI,† the materials with higher crystallinity exhibit a more sluggish and limited leaching process, pointing to the hypothesis that crystallinity and W leaching kinetics show a negative correlation. Moreover, it is believed that the leaching of W could be accelerated if an electrically conductive and large-surface-area substrate is employed to support the bimetal oxides (ESI,† Fig. S52–S54). The metal leaching chemistry is also related to crystal water,[33] leaching agent type (ESI,† Fig. S55) and, possibly, many other factors (ESI,† Note 4). Though enormous experimental efforts were made to explore metal leaching chemistry, controllable experimental and data-driven theoretical studies are needed to achieve a more comprehensive understanding. Based on our as-proposed theories, we offer a concept of reconstructable bi- or multi-component oxide catalyst which can be applied to boost the catalytic activities beyond Ni-catalysed OCORs (ESI,† Fig. S56).

With all the advantages of the catalyst design presented, the practical application potential of $NiWO_4$–TA_{950} as an efficient anode of a urea electrolyser was evaluated in a two-electrode configuration. The device shows superior performance and stability to most of the previously reported electrolysers (ESI,† Fig. S57, S58 and Table S4). Furthermore, we developed a $NiWO_4$–TA_{950}@Pt/C urine electrolyser that successfully decomposed urea while producing H_2, providing an environmentally- and eco-friendly strategy for H_2 production (ESI,† Fig. S57, S59 and S60).

This journal is © The Royal Society of Chemistry 2022

Energy Environ. Sci., 2022, **15**, 2386–2396 | **2393**

Conclusions

In summary, by establishing the dynamic activity–product relationship for alkaline urea electrolysis, for the first time, the unclear and detrimental competition between the OER and the UOR was identified. *Operando* observations and computational studies attributed the performance saturation of the OER and the UOR to the insufficiency of dynamic Ni^{3+} active sites. To boost the dynamic Ni^{3+} population, thus avoiding the OER/UOR performance saturation, a controllable pre-activation approach was presented that considers the electrochemical leaching of tungstate species from pseudo-crystalline $NiWO_4$–TA for the construction of a unique structure with an oxyhydroxide surface layer for better interphase ion transport, a Ni-rich phase for greater redox flexibility, and an intact $NiWO_4$ bulk for mechanical support. The mechanism of the W leaching-induced reconstruction process was observed and elucidated. Further experimental observations suggested that W leaching kinetics can be controlled by manipulating the crystallinity and supporting substrate of the pre-catalyst. With all these observations, we then proposed a concept of reconstructable bi- or multi-component oxide catalysts which can be applied to boost the catalytic activities beyond the Ni-catalysed UOR. In the future, the identification of the OER/OCOR competition and the design of reconstructable metal oxide catalysts can lead to the discovery of new dynamic active site-dominated structure–performance relationship in heterogeneous catalytic systems.

Methods

Chemicals

Nickel(II) chloride hexahydrate ($NiCl_2 \cdot 6H_2O$, $\geq$98%), cobalt(II) chloride hexahydrate ($CoCl_2 \cdot 6H_2O$, 98%), sodium tungstate dihydrate ($Na_2WO_4 \cdot 2H_2O$, $\geq$99%), nickel(II) oxide powder (NiO, 99.8% trace metals basis), tannic acid (ACS reagent), urea (99.0–100.5%), poly(ethylene glycol)-8000 (BioUltra), absolute ethanol (99.8%) and Nafion 117 containing solution ($\sim$5%) were purchased from Sigma Aldrich. Potassium hydroxide (KOH, 85%) was purchased from Fisher Scientific. Hydrophilic carbon paper (TGP-H-060) was purchased from Toray.

Synthesis of $NiWO_4$, $NiWO_4$-TA, $CoWO_4$-PEG, $NiWO_4$–TA@500 and $NiWO_4$–TA@700

$NiWO_4$–TA was prepared by a one-step hydrothermal method. 0.237 g of $NiCl_2 \cdot 6H_2O$, 0.329 g of $Na_2WO_4 \cdot 2H_2O$ and 0.118 g of TA were first dissolved in 45 mL of Milli-Q deionized (DI) water (18.2 MΩ cm) + 15 mL of ethanol. After stirring at room temperature for 30 min, the precursor solution was then transferred to a Teflon-lined stainless-steel autoclave (100 mL) and heated at 160 °C for 12 h. The resultant was centrifuged with water three times (4500 rpm, 10 min) and finally freeze-dried. $NiWO_4$ was manufactured following the same procedures without the addition of TA. $CoWO_4$-PEG was synthesized in a similar way to $NiWO_4$-TA except for different metal and carbon precursors (0.237 g of $CoCl_2 \cdot 6H_2O$ instead of $NiCl_2 \cdot 6H_2O$, and 0.118 g of PEG instead of TA). $NiWO_4$-TA@500 and

$NiWO_4$–TA@700 were obtained by annealing $NiWO_4$–TA under a N_2 atmosphere at 500 and 700 °C, respectively for 2 h at a ramp rate of 10 °C min^{-1}.

Pristine electrode preparation and electrochemical activation

To prepare electrodes for catalysis study, 8 mg of the as-synthesized catalyst was first dispersed in 1 mL of solution that contained 660 μL of DI water, 320 μL of ethanol and 20 μL of 5% Nafion solution. After tip sonication for 5 min, 500 μL of the ink was dropped onto a carbon paper (mass loading $\sim$8 mg cm^{-2}). Electrochemical pre-treatment was performed by CV cycling the as-prepared anodes between 0 and 0.7 V *vs.* Ag/AgCl in 1 M KOH for various cycles.

Electrochemical measurements

Electrochemical measurements were performed using a VSP Biologic potentiostat. Electrochemical tests were carried out using a three-electrode method (unless specified). A graphite rod and saturated Ag/AgCl electrode were used as the counter and reference electrodes, respectively. The as-manufactured pristine/activated electrode was used as the working electrode unless specified. For measurements performed in the RRDE system, the working electrode was prepared as follows. 1 mg of the catalyst was first dispersed in 125 μL of the solution that contained 122.5 μL of ethanol and 2.5 μL of 5% Nafion solution. After tip sonication for 5 min, 25 μL of the ink was dropped onto the disk of a glassy carbon (disk, 0.2475 cm^2)–Au (ring) electrode. LSV and CV were performed at a scan rate of 20 mV s^{-1} unless specified. All potentials were converted to the RHE scale and *iR*-corrected (90%) by the resistance of the electrolyte unless specified. Conversion between the potentials *vs.* RHE and *vs.* saturated Ag/AgCl was performed using the following equation: $E(vs.$ RHE$) = E(vs.$ Ag/AgCl$) + E_{Ag/AgCl}(vs.$ standard hydrogen electrode (SHE)$) + 0.059 \times$ pH. At 25 °C, $E_{Ag/AgCl}$ $(vs.$ SHE$) = 0.197$ V *vs.* SHE. Current densities for all electrochemical measurements were normalized to the geometric surface area of the corresponding current collector used for their respective electrochemical measurement. Electrochemical impedance spectra were recorded at open-circuit voltage under 10 mV of amplitude from 100 kHz to 0.1 Hz.

Physicochemical characterization

The XRD patterns were obtained using a STOE SEIFERT diffractometer with a Mo X-ray radiation source. The HAADF-STEM and EDS analyses were performed using a JEOL JEM ARM200F microscope. The XPS measurements were performed using a Thermo scientific K-alpha photoelectron spectrometer. Data processing of XPS results were achieved by Casa XPS with calibration of adventitious carbon binding energy at 284.8 eV. The ICP-AES test was conducted using an ICP-AES instrument (ICPE-9820, SHIMADZU). The RTMS measurements were performed by connecting the gas outlet of the reaction cell (shown in ESI,† Fig. S9) with a quadrupole mass spectrometer (QGA, Hiden Analytical). An electron energy of 70 eV was used for the ionization of the product species, with an emission current of 100 μA. A flow of Ar was used as the carrier gas.

2394 | *Energy Environ. Sci.*, 2022, **15**, 2386–2396

This journal is © The Royal Society of Chemistry 2022

X-ray absorption spectroscopy

The XANES and XAFS spectra were collected at room temperature at the Diamond Light Source B18 beamline. Measurements of Ni K-edge and W L_3-edge XAFS were carried out using a QEXAFS setup with a fast-scanning Si(111) double crystal monochromator and a Cr-coated branch of collimating and focusing mirrors. The energy ranges for Ni K-edge XAFS and W L_3-edge XAFS were 8133–9183 eV and 10 007–11 034 eV, respectively. Measurements of all *ex situ* samples were performed in both transmission mode and fluorescence mode, while *in situ* experiments were performed only in the fluorescence mode. Self-absorption was evaluated by comparing the fluorescence signal to the transmission signal for both fresh and activated catalysts. For the *operando* experiment, the time resolution is about 150 seconds per spectrum (k_{max} = 16, energy step = 0.3 eV). XAFS spectra were analysed using Demeter software package[34] (including Athena and Artemis software, version 0.9.26) and xraylarch[35] (version 0.9.49) using Python 3.8. Athena software was used for data extraction and XANES analysis of *ex situ* samples. Background subtraction, normalisation and forward Fourier transform of XAFS spectra of *operando* samples are directly processed by xraylarch using the same parameters obtained from a previous Athena project. Linear combination fitting of Ni K-edge XANES spectra was performed by xraylarch using NiOOH and NiWO$_4$ standard material as reference spectra. In addition, Artemis software was used to fit the k^2-weighted EXAFS data. The amplitude reduction factors S_0^2 were calculated to be 0.80 and 0.87 for Ni K-edge and W L_3-edge based on EXAFS analysis of Ni and W foils, respectively, and they are used as fixed parameters in EXAFS analysis.

Computational methods

Calculations of adsorption energy and free energy diagram were performed within the framework of DFT using the Vienna *ab initio* simulation package (VASP) code. Projected augmented wave (PAW) was used for depicting ion–electron interactions.[36] The electronic structures were treated by using the Perdew–Burke–Ernzerhof (PBE) form of the generalized gradient approximation (GGA).[37] Plane wave basis was used with a kinetic cutoff energy of 400 eV. The Monkhorst–Pack meshes of 3 × 3 × 1 were used for k point-sampling in the Brillouin zone.[38] The optimization calculation finished when the force acting on the atom is smaller than 0.05eV Å^{-1}. During the DFT calculations, the model of NiOOH was built by two O–Ni–O layers of NiOOH (001). More information on the construction of the NiWO–W (100) surface is provided in Note S3, ESI.† The generated heterostructure was separated by a 15 Å vacuum layer along the z axis. The formula of adsorption energy (E_{ad}) calculation is as follows: $E_{ad} = E_{system} - E_{substrate} - E_{absorbate}$, where E_{system}, $E_{substrate}$, and $E_{adsorbate}$ represent the total energies of the adsorption system, substrate, and adsorbate respectively. The free energy diagram was calculated by a method reported in a previous study.[39] The electrochemical process of the oxygen evolution reaction in alkaline media can be divided into four one-electron reactions as follows: $* + 4OH^- \rightarrow *OH +$

$3OH^- + e^- \rightarrow *O + H_2O + 2OH^- + 2e^- \rightarrow *OOH + H_2O + OH^- + 3e^- \rightarrow * + 2H_2O + O_2 + 4e^-$, in which * represents an active catalytic site. The Gibbs free energy of each states is calculated using the equation: $G = E + ZPE - TS - eU$, in which G, E, ZPE, S and U represent Gibbs free energy, DFT-based thermal energy, zero-point energy, entropy and applied potential (*vs.* NHE). The energy of OH^- can be calculated using the equation: $G(OH^-) = G(H_2O) - G(H^+) = G(H_2O) - (1/2G(H_2) - RT\ln10 \times pH)$, in which R is the ideal gas constant, T is the temperature in Kelvin and pH is assumed to be 14. In this regard, the free energy change of the total reaction ($4OH^- \rightarrow 2H_2O + O_2 + 4e^-$) is calculated to be 0.404 eV, which is different from that of the acidic OER ($2H_2O \rightarrow O_2 + 4H^+ + 4e^-$, ΔG = 1.23 eV).

Simulation of the W leaching mechanism was performed by utilizing CRYSTAL17.[40] The basis set was downloaded from CRYSTAL website (http://www.crystal.unito.it/basis-sets.php). All electron basis set were used for Ni (Ni_86-411(41d)G_towler_1992) and O (O_8-411(1d)G_baranek_2013_BaTiO$_3$). Effective core pseudopotentials were used in the W basis set (W_cora_1996). The exchange–correlation functional was chosen as PBE0 (including 25% Hartree–Fock exchange). The $\mathbf{k}$-mesh was set to be 8 × 8 × 8. The ferromagnetic (FM) and non-magnetic (NM) phases of NiWO$_4$ were optimised by keeping all the crystal symmetry. The crystal structure of NiWO$_4$ were obtained from Crystallography Open Database (www.crystallography.net, ID: 8103678), with the space group $P12/c1$ and cell parameters of a = 4.5992 Å, b = 5.6606 Å, c = 4.9068 Å, and β = 90.3. Please see the ESI,† (Note S3) for more details.

Author contributions

R. L. and G. H. conceived the project and designed the experiments; R. L. synthesized the materials and performed characterisation and electrocatalytic studies; L. K., V. C. and G. C. carried out spectroscopy studies and analysed the data; T. Z., J. F. and F. C. performed DFT calculations; G. Z. and A. K. performed the MS experiment; I. P. supported with XPS and XRD characterisation; G. H. directed the project; D. B., F. C. and G. H. supervised the project; R. L., L. K., T. Z., J. F. and G. H. wrote the manuscript and all authors revised the manuscript.

Conflicts of interest

There are no conflicts to declare.

Acknowledgements

This journal is © The Royal Society of Chemistry 2022

Energy Environ. Sci., 2022, **15**, 2386–2396 | **2395**

References

1 Q. Wang, M. Nakabayashi, T. Hisatomi, S. Sun, S. Akiyama, Z. Wang, Z. Pan, X. Xiao, T. Watanabe, T. Yamada, N. Shibata, T. Takata and K. Domen, *Nat. Mater.*, 2019, **18**, 827–832.

2 S. T. Thompson and D. Papageorgopoulos, *Nat. Catal.*, 2019, **2**, 558–561.

3 S. Zhao, J. Berry-Gair, W. Li, G. Guan, M. Yang, J. Li, F. Lai, F. Corà, K. Holt, D. J. L. Brett, G. He and I. P. Parkin, *Adv. Sci.*, 2020, **7**, 1903674.

4 D. Y. Chung, P. P. Lopes, P. Farinazzo, B. D. Martins, H. He, T. Kawaguchi, P. Zapol, H. You, D. Tripkovic, D. Strmcnik, Y. Zhu, S. Seifert, S. Lee, V. R. Stamenkovic and N. M. Markovic, *Nat. Energy*, 2020, **5**, 222–230.

5 S. Song, J. Zhou, X. Su, Y. Wang, J. Li, L. Zhang, G. Xiao, C. Guan, R. Liu, S. Chen, H.-J. Lin, S. Zhang and J.-Q. Wang, *Energy Environ. Sci.*, 2018, **11**, 2945–2953.

6 H. Dotan, A. Landman, S. W. Sheehan, K. D. Malviya, G. E. Shter, D. A. Grave, Z. Arzi, N. Yehudai, M. Halabi, N. Gal, N. Hadari, C. Cohen, A. Rothschild and G. S. Grader, *Nat. Energy*, 2019, **4**, 786–795.

7 X. Cui, P. Xiao, J. Wang, M. Zhou, W. Guo, Y. Yang, Y. He, Z. Wang, Y. Yang, Y. Zhang and Z. Lin, *Angew. Chem., Int. Ed.*, 2017, **56**, 4488–4493.

8 M. Song, Z. Zhang, Q. Li, W. Jin, Z. Wu, G. Fu and X. Liu, *J. Mater. Chem. A*, 2019, **7**, 3697–3703.

9 L. Zhang, L. Wang, H. Lin, Y. Liu, J. Ye, Y. Wen, A. Chen, L. Wang, F. Ni, Z. Zhou, S. Sun, Y. Li, B. Zhang and H. Peng, *Angew. Chem., Int. Ed.*, 2019, **58**, 16820–16825.

10 W. Chen, L. Xu, X. Zhu, Y.-C. Huang, W. Zhou, D. Wang, Y. Zhou, S. Du, Q. Li, C. Xie, L. Tao, C.-L. Dong, J. Liu, Y. Wang, R. Chen, H. Su, C. Chen, Y. Zou, Y. Li, Q. Liu and S. Wang, *Angew. Chem., Int. Ed.*, 2021, **60**, 7297–7307.

11 S.-K. Geng, Y. Zheng, S.-Q. Li, H. Su, X. Zhao, J. Hu, H.-B. Shu, M. Jaroniec, P. Chen, Q.-H. Liu and S.-Z. Qiao, *Nat. Energy*, 2021, **6**, 904–912.

12 J. Li, J. Li, T. Liu, L. Chen, Y. Li, H. Wang, X. Chen, M. Gong, Z.-P. Liu and X. Yang, *Angew. Chem., Int. Ed.*, 2021, **60**, 26656–26662.

13 J. Suntivich, K. J. May, H. A. Gasteiger, J. B. Goodenough and Y. Shao-Horn, *Science*, 2011, **334**, 1383–1385.

14 M. Bajdich, M. García-Mota, A. Vojvodic, J. K. Nørskov and A. T. Bell, *J. Am. Chem. Soc.*, 2013, **135**, 13521–13530.

15 N. Zhang, X. Feng, D. Rao, X. Deng, L. Cai, B. Qiu, R. Long, Y. Xiong, Y. Lu and Y. Chai, *Nat. Commun.*, 2020, **11**, 4066.

16 T. Wu, S. Sun, J. Song, S. Xi, Y. Du, B. Chen, W. A. Sasangka, H. Liao, C. L. Gan, G. G. Scherer, L. Zeng, H. Wang, H. Li, A. Grimaud and Z. J. Xu, *Nat. Catal.*, 2019, **2**, 763–772.

17 H. Huang, C. Yu, H. Huang, C. Zhao, B. Qiu, X. Yao, S. Li, X. Han, W. Guo, L. Dai and J. Qiu, *Nano Energy*, 2019, **58**, 778–785.

18 B. Zhang, K. Jiang, H. Wang and S. Hu, *Nano Lett.*, 2019, **19**, 530–537.

19 R. P. Forslund, J. T. Mefford, W. G. Hardin, C. T. Alexander, K. P. Johnston and K. J. Stevenson, *ACS Catal.*, 2016, **6**, 5044–5051.

20 Z. Jiang, W. Sun, H. Shang, W. Chen, T. Sun, H. Li, J. Dong, J. Zhou, Z. Li, Y. Wang, R. Cao, R. Sarangi, Z. Yang, D. Wang, J. Zhang and Y. Li, *Energy Environ. Sci.*, 2019, **12**, 3508–3514.

21 Z. Qiao, S. Hwang, X. Li, C. Wang, W. Samarakoon, S. Karakalos, D. Li, M. Chen, Y. He, M. Wang, Z. Liu, G. Wang, H. Zhou, Z. Feng, D. Su, J. S. Spendelow and G. Wu, *Energy Environ. Sci.*, 2019, **12**, 2830–2841.

22 G. Zhang and A. Kucernak, *ACS Catal.*, 2020, **10**, 9684–9693.

23 D. Chen and S. D. Minteer, *J. Power Sources*, 2015, **284**, 27–37.

24 M. Bernicke, E. Ortel, T. Reier, A. Bergmann, J. Ferreira de Araujo, P. Strasser and R. Kraehnert, *ChemSusChem*, 2015, **8**, 1908–1915.

25 H. B. Tao, Y. Xu, X. Huang, J. Chen, L. Pei, J. Zhang, J. G. Chen and B. Liu, *Joule*, 2019, **3**, 1498–1509.

26 J. Wang, L. Gan, W. Zhang, Y. Peng, H. Yu, Q. Yan, X. Xia and X. Wang, *Sci. Adv.*, 2018, **4**, eaap7970.

27 Z.-F. Huang, J. Song, Y. Du, S. Xi, S. Dou, J. M. V. Nsanzimana, C. Wang, Z. J. Xu and X. Wang, *Nat. Energy*, 2019, **4**, 329–338.

28 M. Steimecke, G. Seiffarth, C. Schneemann, F. Oehler, S. Förster and M. Bron, *ACS Catal.*, 2020, **10**, 3595–3603.

29 H.-Y. Wang, Y.-Y. Hsu, R. Chen, T.-S. Chan, H. M. Chen and B. Liu, *Adv. Energy Mater.*, 2015, **5**, 1500091.

30 G. Karkera, T. Sarkar, M. D. Bharadwaj and A. S. Prakash, *ChemCatChem*, 2017, **9**, 3681–3690.

31 L. Wang, Y. Zhu, Y. Wen, S. Li, C. Cui, F. Ni, Y. Liu, H. Lin, Y. Li, H. Peng and B. Zhang, *Angew. Chem., Int. Ed.*, 2021, **60**, 10577–10582.

32 S. Anantharaj, H. Sugime and S. Noda, *ACS Appl. Energy Mater.*, 2020, **3**, 12596–12606.

33 X. Liu, J. Meng, K. Ni, R. Guo, F. Xia, J. Xie, X. Li, B. Wen, P. Wu, M. Li, J. Wu, X. Wu, L. Mai and D. Zhao, *Cell Rep. Phys. Sci.*, 2020, **1**, 100241.

34 B. Ravel and M. Newville, *J. Synchrotron Radiat.*, 2005, **12**, 537–541.

35 M. Newville, *J. Phys.: Conf. Ser.*, 2013, **430**, 012007.

36 P. E. Blöchl, *Phys. Rev. B: Condens. Matter Mater. Phys.*, 1994, **50**, 17953–17979.

37 J. P. Perdew, K. Burke and M. Ernzerhof, *Phys. Rev. Lett.*, 1996, **77**, 3865–3868.

38 H. J. Monkhorst and J. D. Pack, *Phys. Rev. B: Solid State*, 1976, **13**, 5188–5192.

39 J. K. Nørskov, J. Rossmeisl, A. Logadottir, L. Lindqvist, J. R. Kitchin, T. Bligaard and H. Jónsson, *J. Phys. Chem. B*, 2004, **108**, 17886–17892.

40 R. Dovesi, A. Erba, R. Orlando, C. M. Zicovich-Wilson, B. Civalleri, L. Maschio, M. Rérat, S. Casassa, J. Baima, S. Salustro and B. Kirtman, *Wiley Interdiscip. Rev.: Comput. Mol. Sci.*, 2018, **8**, e1360.

2396 | *Energy Environ. Sci.*, 2022, **15**, 2386–2396

This journal is © The Royal Society of Chemistry 2022